Investigation of the Reaction $\pi^- p \to \omega^0 n$ at 3.65, 4.50, and 5.50 GeV/c *

L. E. Holloway, B. Huld,† M. Jordan,‡ D. W. Mortara,§ E. I. Rosenberg,|| and A. D. Russell**
Department of Physics, University of Illinois at Urbana-Champaign, Urbana, Illinois 61801

S. Bernstein, M. H. Garrell,†† S. Margulies, and D. W. McLeod
Department of Physics, University of Illinois at Chicago Circle, Chicago, Illinois 60680
(Received 30 May 1973)

An experiment using optical spark chambers and a neutron time-of-flight hodoscope has been performed at the Argonne National Laboratory on the reaction $\pi^- p \to \omega^0 n$. The differential cross section and the experimentally accessible density-matrix elements were determined in the momentum transfer interval $0.05 \leq |t| \leq 1.0$ (GeV/c)^2 at each of three incident pion momenta 3.65, 4.50, and 5.50 GeV/c. Our results show the following general features: (1) a dip in the forward differential cross section for $|t| \leq 0.2$ (GeV/c)^2, (2) a slope at larger momentum transfers which increases as the incident pion momentum increases, and (3) no dips in either $d\sigma/dt$ or $\rho_{11} + \rho_{1-1}$, the natural-parity exchange combination, at $|t| = 0.6$ (GeV/c)^2.

I. INTRODUCTION

In an attempt to elucidate production mechanisms in quasi-two-body processes we have investigated the reaction

$$\pi^- p \to \omega^0 n, \quad \omega^0 \to \pi^+\pi^-\pi^0, \quad \pi^0 \to \gamma\gamma$$

at incident pion momenta of 3.65, 4.50, and 5.50 GeV/c in a counter–optical-spark-chamber experiment performed at the Zero Gradient Synchrotron (ZGS) at Argonne National Laboratory. The experiment consisted of determining both the differential cross section $d\sigma/dt$ and the experimentally accessible ω^0 spin-density matrix elements ρ_{ij} over the momentum-transfer interval $0.05 \leq |t| \leq 1.0$ (GeV/c)^2 at each of the three beam momenta. A report on the spin-density matrix elements has been published elsewhere.[1]

The reaction in question is very appealing for analysis in terms of peripheral—especially Regge—models. Conservation of isospin and of G parity restrict the quantum numbers which may be exchanged in the t channel in this reaction to $I^G = 1^+$. Of the known low-lying meson states, only the $\rho(765)$, with $J^P = 1^-$, and the $B(1234)$, with $J^P = 1^+$, have the proper quantum numbers. In terms of Regge models, only one natural-parity trajectory, the ρ, and one unnatural-parity trajectory, the B, may be exchanged. It is well known that for vector-meson production in reactions of the form π + baryon → vector meson + baryon, the helicity-zero state of the vector meson can be populated only by an unnatural-parity t-channel exchange.[2] It has also been shown by Ader *et al.* and Hogaasen *et al.*[3] that appropriate linear combinations of the spin-density matrix elements of the vector meson isolate the natural- and unnatural-parity contributions to the scattering amplitude in the limit of high energy. In ω^0 production, only one low-lying exchange of each type is allowed, and a particularly clean separation of these effects may be expected.

The reaction in question is well suited to counter–spark-chamber investigations rather than to the use of low-density liquid bubble chambers. The presence of multiple neutral particles in the final state of the reaction $\pi^- p \to \omega^0 n$ forces bubble-chamber experiments to study the charge-symmetric reaction $\pi^+ n \to \omega^0 p$ in the form $\pi^+ d \to \omega^0 p (p_s)$.[4-11] These experiments are limited statistically by the inability to trigger most bubble chambers, and also involve the problems of clearly identifying the spectator protons and of normalizing the low-$|t|$ region because of the Pauli exclusion principle.

In this report, the experimental details are presented in Sec. II, the data analysis in Sec. III, and the results and conclusions in Sec. IV.

II. EXPERIMENTAL DETAILS

The experiment was performed in the 17° beam at the Argonne ZGS. The apparatus, consisting essentially of a liquid-hydrogen target, thin-foil optical spark chambers to detect the charged pions, thick-plate optical spark chambers to detect the γ's, and a neutron-counter hodoscope with time-of-flight determination to measure the neutron momentum, is shown in Figs. 1 and 2.

The unseparated π^- beam, produced from an internal target, was brought to a spot 13 mm high by 32 mm wide at the liquid-hydrogen target. The beam divergence half-angles were 7 mr vertically and 4 mr horizontally. A slit defining the momentum resolution, as well as the intensity, was lo-

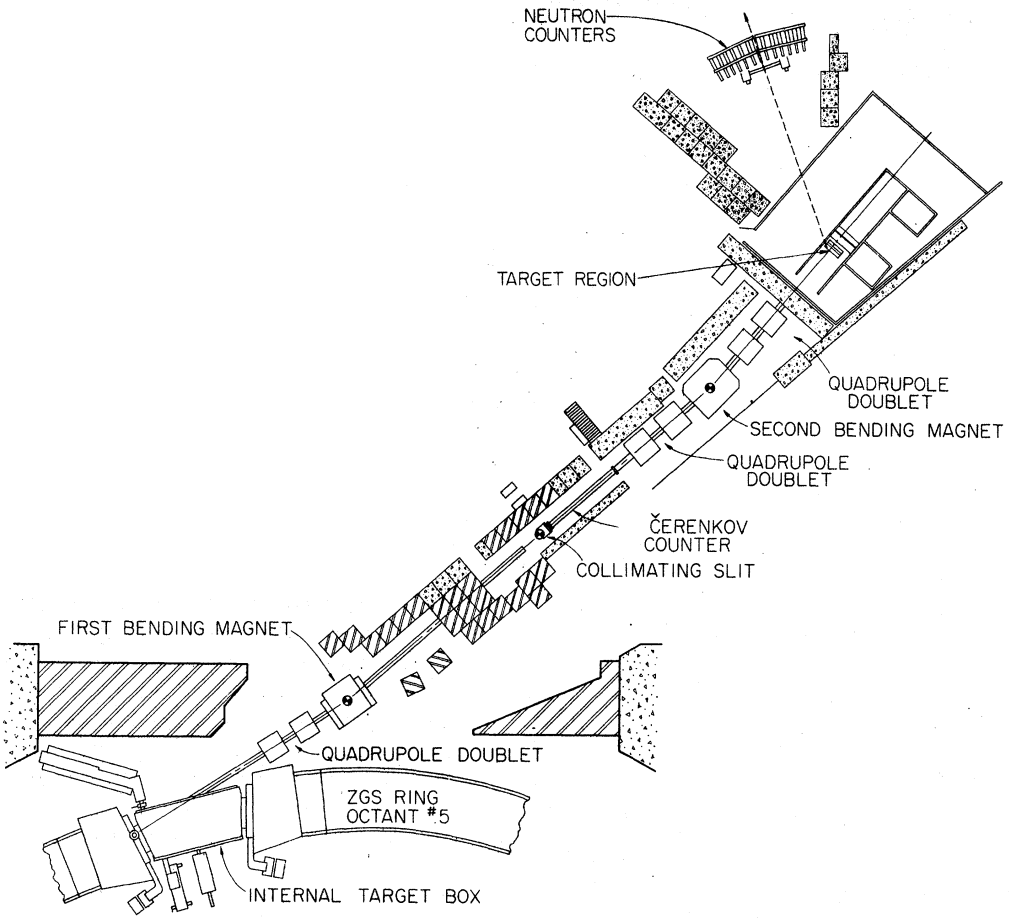

FIG. 1. Floor plan of experimental layout.

cated directly upstream of a Freon Čerenkov counter employed to veto electrons. For most of the data, the momentum bite was $\pm\frac{3}{4}\%$; at the widest slit opening, the momentum spread increased to $\pm 1\%$. In separate runs, the beam transport system was adjusted for central momenta of 3.65, 4.50, and 5.50 GeV/c. Counting rates in the beam telescope (counters B_0, B_1, and B_2) were maintained between 100 000 and 200 000 particles spread over a 450 to 500 ms spill time, with a repetition rate of about 16 pulses/min. The liquid-hydrogen target was a cylinder 30 cm long and 5 cm in diameter.

A detailed view of the target region in shown in Fig. 2. The incident beam was defined by a telescope consisting of counters B_0, B_1, B_2, and HA; counter B_1 also served to generate the "start" signal for the neutron time-of-flight measurement. A beam-anticoincidence counter, BA, vetoed events having a charged track in the beam line downstream from the target. The target was surrounded on five sides by a box of anticoincidence counters, HA and SA_1 through SA_5, to veto any event having charged particles at angles too large to be consistent with ω^0 production and subsequent decay. A hole in counter HA provided beam entrance. Five additional counters, WA_1 through WA_5 (not shown), defined the fiducial area on the downstream face of the box.

The downstream face of the target box was closed by two thin-foil optical spark chambers, TF_1 and TF_2, used to identify the charged pions. These chambers had a fiducial area 69 cm by 69 cm, and had four 1-cm-wide gaps each. A pion hodoscope, π_1 through π_{17}, consisting of seventeen horizontal scintillator strips was placed downstream of TF_2. Signals from two, and only two, of these counters were required in a valid event trigger. Two thick-plate shower chambers, SC_1 and SC_2, served the dual purpose of providing additional information on the directions of the charged tracks and of determining the conversion vertices of the gammas produced from π^0 decay. Each chamber had 20 1-cm-wide gaps and an active area 91 cm high by 122 cm wide. To yield useful information regarding the charged track

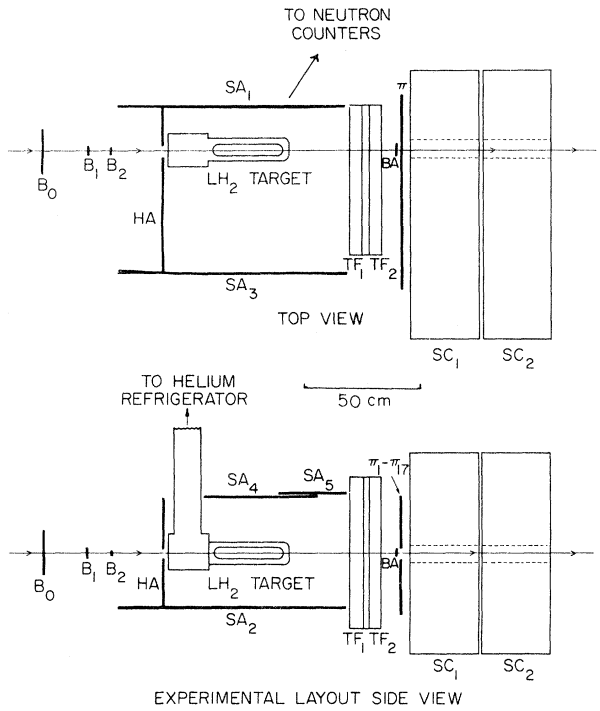

FIG. 2. Detailed views of the target region.

directions, the first 7 plates in SC_1 were 3.1-mm-thick aluminum, while all subsequent plates, in both chambers, were aluminum-lead-aluminum sandwiches (0.76 mm Al, 1.52 mm Pb, 0.76 mm Al) in order to provide a high γ-ray conversion probability. These sandwich plates presented about 10.0 radiation lengths of material for conversion of the photons. A 76-mm-diameter hole through the center of the chambers allowed for passage of beam particles.

All spark chambers were viewed from the top and side using a 90° stereo optical system. Both top and side views were folded onto a double 35-mm frame using front-aluminized mirrors. The camera was a Flight Research[12] model 207 fitted with a 150-mm lens used at f/11.

A 52-element neutron-counter hodoscope with time-of-flight determination, located 10 m from the target (see Fig. 1), was employed to measure the neutron momentum. The detector elements consisted of 10-cm-wide by 25-cm-high by 30-cm-deep blocks of NE 102 plastic scintillator[13] arranged in an array 4 counters high by 13 counters wide. The entire hodoscope could rotate about the target, and its position was adjusted to cover the range $0.04 \leq |t| \leq 1.0$ $(\mathrm{GeV}/c)^2$ for each of the three incident beam momenta. Since the horizontal spacing between centers of the hodoscope elements was approximately three counter widths, data taking was performed using a three-run sequence. An initial run was made with the hodoscope centered; then the hodoscope was displaced left and right one counter width from the central position on two subsequent runs. This procedure ensured a continuous angular acceptance.

Event selection was determined by neutron counter logic, time-of-flight logic, and trigger logic systems. The electronics employed were a combination of EG& G,[14] Lecroy,[15] and University of Illinois fast-logic modules.

Four 50-Ω signals, two from the anode and one each from the 13th and 14th dynodes, were available from the 58AVP phototube used in each neutron counter. These signals were used to determine the neutron's scattering angle θ, its time of flight (TOF), the azimuthal angle of the scattering plane, ϕ, and the pulse height. Within each column of 4 counters, one set of anode signals was passively added to provide 13 TOF signals; similarly, the (inverted) outputs from the 14th dynodes provided 13 θ signals. Along each row of 13 counters, the remaining anode outputs were passively added to yield four ϕ signals. The remaining 52 outputs (from the 13th dynodes) were added passively for pulse-height information.

The 13 TOF signals were fed into 13 discriminators set with very low thresholds (about 1 MeV energy loss in the counter). The 13 θ signals were fed into 13 additional discriminators, but with a much higher threshold setting (about 6 MeV energy loss). The output of the θ discriminators was much wider (20 ns) than that of the TOF discriminators (5 ns), and the TOF signal was approximately centered on the θ signal. A coincidence between θ and TOF signals then generated timing information defined by the TOF signal. This high-low discrimination technique was used to minimize the effect of slewing on the time-of-flight measurement, and, at the same time, to effectively discriminate against the low-energy neutron background prevalent at the ZGS. The time of flight was digitized using a time-to-amplitude converter followed by an analog-to-digital converter. A "start" signal was provided by counter B_1, as mentioned previously; a "stop" signal consisted of a gated TOF pulse, as described above. The rms error in the time-of-flight measurement was determined to be 0.85 ns.

To select events having only two charged particles in the pion hodoscope (counters π_1 through π_{17}), the outputs from 17 hodoscope elements were passively added and then passed through a differential discriminator. The output of this discriminator constituted the 2π signal, an indication that two, and only two, pion-hodoscope elements had fired.

A valid event trigger was defined electronically

by the logical requirement $(B_0B_1B_2)(2\pi)(\theta)\bar{\bar{C}}\,\overline{BA}\,\overline{HA}\,\overline{SA}\,\overline{WA}$, where the counters are shown in Figs. 1 and 2, and their nomenclature is given above. The coincidence $(B_0B_1B_2)$ denotes a valid incident beam particle; the (2π) signal indicates two, and only two, charged particles emerging in the forward direction; (θ) represents a valid signal from the neutron hodoscope; $\bar{\bar{C}}$ denotes the absence of a veto by the Freon threshold Čerenkov counter, indicating that the beam particle is a pion; and $\overline{BA}\,\overline{HA}\,\overline{SA}\,\overline{WA}$ ensures that no charged particles have emerged from the anticoincidence box surrounding the target. This event trigger initiated the following sequence of events: The spark chambers were fired, certain identifying information was displayed on binary coded lights for photographic recording and also placed on a data bus, and the camera was advanced. The coded information consisted of run and event numbers, neutron time of flight, neutron-counter pulse height, and θ and ϕ indices for the neutron counter hit. Multiple θ or ϕ hits were flagged and accepted. The indices of the two pion hodoscope counters which fired were also transmitted on the data bus.

The data bus transmitted information to an on-line XDS $\Sigma 2$ computer.[16] A Kennedy incremental tape recorder[17] was used as a back-up for, and occasionally in addition to, the computer. The on-line computer performed several functions: to buffer the transmission of the identifying information from data bus to magnetic tape, to perform preliminary calculations from these data, to write these results together with the identifying information on magnetic tape, and to accumulate a wide variety of histograms used to monitor the progress of the experiment.

The high data-taking rate of the computer was employed to monitor the calibration of the time-of-flight electronics. (During normal operation, the data-taking rate was limited by the camera recycle time.) About once every six runs, the camera and spark chambers were disabled, the timing gates of the neutron counters were changed, and a high-statistics run was made detecting γ rays from events $\pi^- p \to \gamma +$ anything in the neutron hodoscope. These "prompt peaks" were used to define the zero for the time-of-flight scale.

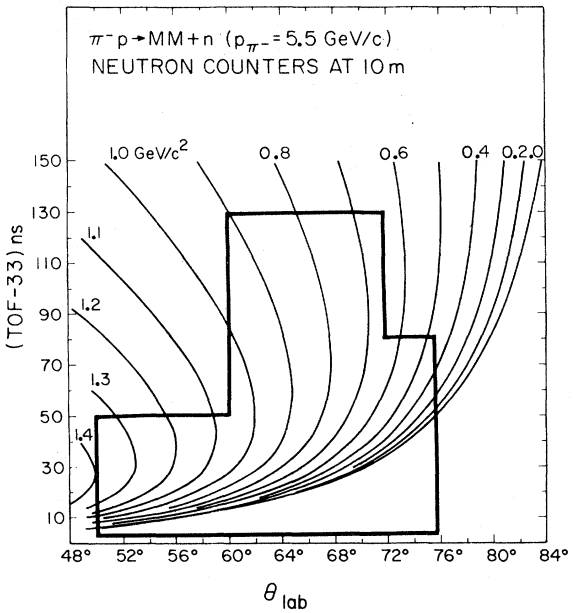

FIG. 3. Neutron time of flight vs laboratory angle for a series of missing masses in the reaction $\pi^- p \to n$ + (missing mass). The acceptance limits defined by the timing gates are outlined.

III. DATA ANALYSIS

A. Prescanning Event Selection

A total of 134 800, 142 700, and 148 100 events were recorded at 3.65, 4.50, and 5.50 GeV/c incident pion momenta, respectively. In collecting these data, the missing-mass and momentum-transfer regions accepted for an event were kinematically constrained. This was accomplished electronically by employing the neutron-counter angles and time-of-flight gates (different for each column of four counters at a common angle θ). The acceptance was set generously large in order to avoid biases and to allow an adequate comparison with data away from the ω^0 region. The acceptance, at the highest beam momentum, 5.50 GeV/c, is shown in Fig. 3. As can be seen in Fig. 4, which gives the mass resolution of spectrometer at 4.5 GeV/c as a function of momentum transfer, the mass acceptance at larger $|t|$ values (smaller times of flight) is large. Thus,

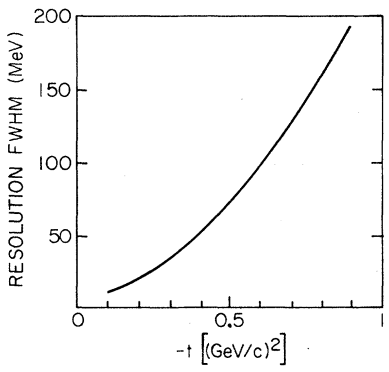

FIG. 4. Resolution full width at half maximum (FWHM) of the neutron missing-mass spectrometer at 4.50 GeV/c as a function of momentum transfer.

TABLE I. Definition of control regions and ω-mass regions as a function of momentum transfer. These defined mass regions are independent of incident energy.

$\lvert t\rvert$ [(GeV/c)^2]	Low control (GeV/c^2)	ω mass (GeV/c^2)	High control (GeV/c^2)
0.05–0.10	0.70–0.75	0.75–0.81	0.81–0.86
0.10–0.20	0.68–0.75	0.75–0.83	0.83–0.90
0.2–0.3	0.65–0.73	0.73–0.83	0.83–0.91
0.3–0.5	0.63–0.73	0.73–0.85	0.85–0.95
0.5–0.7	0.58–0.71	0.71–0.87	0.87–1.00
0.7–1.0	0.57–0.71	0.71–0.88	0.88–1.02

procedures to reduce the number of spark-chamber pictures to be scanned become desirable.

To this end, the raw data were subjected to cuts, based upon on-line-computer-recorded data. The first cut eliminated those events which gave an unphysical value for the missing mass. Approximately 32% of the film was processed with just this cut. Of the remaining 68% of the film, an event was scanned if the time of flight and scattering angle were within four standard deviations of the ω^0 mass curve. (That is, an ellipse with semiaxes of 76 mr in θ and 6 ns in TOF was constructed for each event, and the event was accepted if the computed ω^0 mass curve passed through this ellipse.) In addition, all events with missing mass between 540 and 1030 MeV/c^2 were scanned. These requirements rejected about half of the raw events.

As a test of this procedure, approximately 800 2γ events were processed using both cuts. A corrected spectrometer mass based on the event vertex, updated time-of-flight calibration, and surveyed counter positions was calculated. These results showed that no events with a corrected mass in the range 560 to 1000 MeV/c^2 were excluded by the stronger cuts, thus validating the procedures used. The final data, however, include some events outside this range; these events are primarily due to the 32% of the data which were processed without the stronger mass cut. Additional contributions come from those events of the larger strong-cut data sample which had relatively large mass errors due to the decreasing mass resolution at large values of $\lvert t\rvert$ (i.e., small times of flight).

B. Scanning, Measuring, and Event Reconstruction

The events which survived the cutting procedures described in the preceding section were visually scanned and grouped into five classes: (1) chamber breakdowns (~2%); (2) zero-shower events (~52%); (3) one-shower events (~21%); (4) two-shower events (~18%); and (5) more-than-two-shower events (~7%). A shower was defined to have at least 5 associated sparks in both top and side views, to have no sparks in the thin-foil chambers, and not to point back to a secondary interaction. Additional criteria allowed the scanners to distinguish charged tracks which were not visible in the foil chambers from showers. The fraction of events in the five categories was essentially the same at each of the three beam momenta. A portion (~22%) of the film was rescanned, and conflicts between the two scans were resolved. From these investigations, we estimate the single-scan efficiency for detecting two-shower events to be about 70%.

After scanning, 15 800, 11 700, and 11 200 events at 3.65, 4.50, and 5.50 GeV/c, respectively, remained as two-shower candidates to be submitted for measurement. At this point, additional selection occurred as the measurers rejected improperly classified events and events such as those whose production vertices were obviously not in the target. Accepted two-shower events were measured on a University of Illinois scanning and measuring projector (SMP).[18] The measurements digitized the reprojected image-plane positions of the top- and side-view coordinates of the sparks defining the two charged-particle paths, the top- and side-view coordinates of the first spark in each shower,

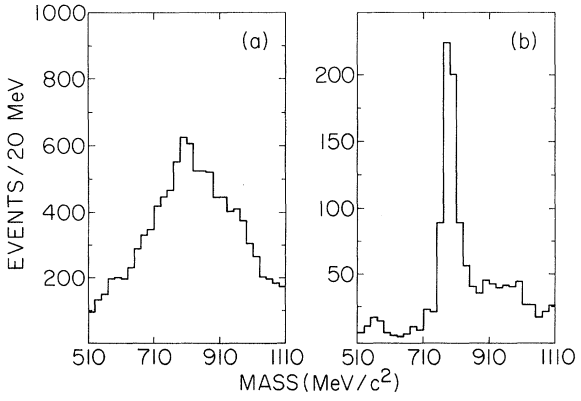

FIG. 5. Mass spectra at P_{lab} = 4.50 GeV/c showing the improvement in signal-to-noise ratio due to kinematic fitting: (a) two-shower events submitted for measuring and (b) final data sample. The results at P_{lab} = 3.65 and 5.50 GeV/c are similar.

and a set of four fiducial crosses generated by electroluminescent panels attached to the spark chambers.

The measured two-shower events were reconstructed in space using a least-squares fitting routine. The optical constants necessary to effect the transformation from film plane to laboratory coordinates were determined from a set of 120 fiducial marks which were fixed to the spark chambers and which were surveyed relative to the laboratory coordinates. The four fast fiducial crosses were photographed with each event and, every hundred frames, with the full set of 120 cross-hair fiducials. The optical constants describing the transformation from the SMP image plane to the film plane were independently monitored biweekly during the measuring period.

The SMP image-plane coordinates of the measured points were transformed to space coordinates. A least-squares fit was then attempted to determine the event vertex from the intersection of the two charged tracks. The directions of the γ's were obtained from the fitted-event vertex and the measured positions of the first spark of each shower. The event vertex and the position of the neutron counter which fired determined the neutron's direction. The quantities supplied by this analysis program were the direction cosines of all five final-state particles and the three coordinates, with errors, of the event vertex.

The results from the geometric reconstruction and the electronically measured neutron time of flight were used as input to another least-squares fitting program. This program attempted a kinematic fit to the one-constraint hypothesis $\pi^- p \to \pi^+ \pi^- \pi^0 n$. The effect of the kinematic fitting procedure on the signal-to-noise ratio is shown in Fig. 5, where the mass spectra (at 4.50 GeV/c) of events submitted for measuring as two-shower events and the final data sample are plotted. The results at 3.65 GeV/c and 5.50 GeV/c are comparable to those shown.

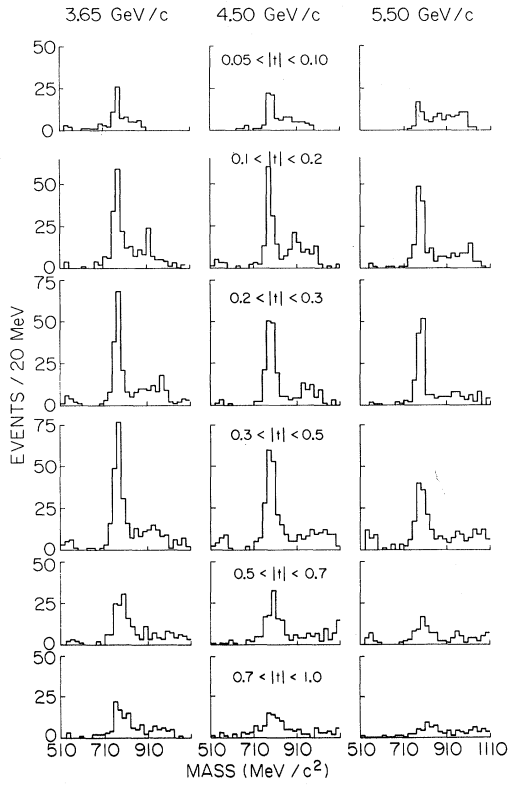

FIG. 6. Mass spectra of final data samples.

C. Selection of Final Data Sample

A series of cuts on the results of the kinematic fitting produced the final data sample. These cuts required the fitted event to have:

(1) a χ^2 value equal to or less than 16;

(2) an energy imbalance of less than 5 MeV between initial and final states;

(3) both photon energies greater than 80 MeV; and

(4) consistency with the pion hodoscope and anticoincidence-counter geometries.

For each momentum-transfer interval, ω^0 and control mass regions were defined as shown in Table I. The corresponding mass spectra are shown in Fig. 6. The final data sample, after a

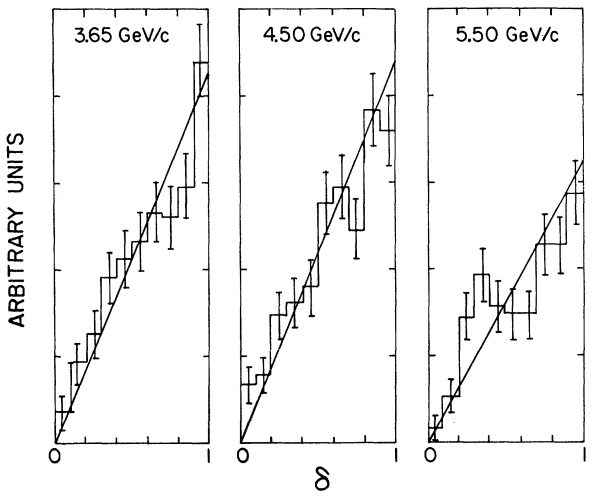

FIG. 7. The radial-Dalitz-plot density, i.e., the number of events after background subtraction vs $\delta = |\vec{p}_1 \times \vec{p}_2|^2 / |\vec{p}_1 \times \vec{p}_2|^2_{max}$, where $\vec{p}_1$ and $\vec{p}_2$ are the momenta of the charged pions in the ω rest frame. The straight line corresponds to the distribution expected from a decay amplitude $M \propto |\vec{p}_1 \times \vec{p}_2|$.

linear background subtraction, contained 567 ω^0 events at 3.65 GeV/c, 562 at 4.50 GeV/c, and 395 at 5.50 GeV/c.

In Fig. 7 the number of events after background subtraction is plotted vs the radial-Dalitz-plot variable δ given by

$$\delta = |\vec{p}_1 \times \vec{p}_2|^2 / |\vec{p}_1 \times \vec{p}_2|^2_{\max} ,$$

where $\vec{p}_1$ and $\vec{p}_2$ are the momenta of the charged pions in the ω^0 rest frame. The results are in agreement with the expected straight-line distributions. The events in the control region do not show this behavior as seen in Fig. 8. We conclude that the subtracted distributions represent relatively pure ω^0 samples.

D. Experimental Biases

There are two main contributions to experimental biases: (1) the geometric acceptance of the pions, which affects the determination of the density matrix elements and to a lesser extent the relative differential cross section, and (2) the variation of the neutron-detection efficiency with neutron kinetic energy, which affects the determination of the differential cross section but does not affect the determination of the density matrix elements.

A net detection efficiency, momentum-transfer-dependent, was defined by

$$\epsilon_{\text{net}} = \prod \epsilon_i ,$$

where the ϵ_i are individual efficiencies described below. Figure 9 shows ϵ_{net} as a function of momentum transfer.

To examine losses due to inefficiencies in the kinematic fitting program, a Monte Carlo study (5000 events at each energy) was made. The generated events were assigned errors corresponding to the known measurement errors and were then processed by the fitting program. The efficiency of the fitting program, ϵ_{prog}, varied smoothly with t from about 85% at $|t| = 0.05$ (GeV/c)^2 to 95% at $|t| = 1.0$ (GeV/c)^2.

The geometric acceptance of the meson arm of the experiment (the spark chambers and all counters except the neutron-counter hodoscope) for 2γ events can be factored into two terms. The first, $\epsilon_{2\pi}$, gives the geometric efficiency for detecting the two charged pions. The second, $\epsilon_{2\gamma}$, is the efficiency for detecting the photon conversion showers given two detected pions. The product $\epsilon_{2\pi}\epsilon_{2\gamma}$ showed a t dependence which varied smoothly from about 50% at small $|t|$ to 65% at $|t| = 1$ (GeV/c)^2.

In the neutron-counter hodoscope the vertical banks of 4 counters were separated by 2 counter widths. This separation gave rise to an average acceptance of about $\frac{1}{3}$. A direct calculation of this acceptance, ϵ_{NC}, which included effects of the finite target length and the neutron-counter geometry showed that it varied only slightly with the neutron's laboratory angle, i.e., with t.

A calculation of the losses caused by secondary neutron interactions occurring between the event vertex and the neutron counters showed that the corresponding efficiency, ϵ_{NI}, varied from 85% to 96% as t varied from 0.05 to 1.0 (GeV/c)^2.

The efficiencies, $\epsilon_{\gamma_{\text{CONV}}}$ and ϵ_δ, account for losses due to photon conversions and pion-induced δ rays resulting in a third, i.e., vetoing, count in the pion hodoscope. These losses were calculated to be 12% and 15%, respectively.

A high-statistics (30 000 events at each energy) Monte Carlo study assuming unaligned ω's was used to study an apparent alignment induced by processing the events through the standard energy and geometry cuts. This alignment exhibited a

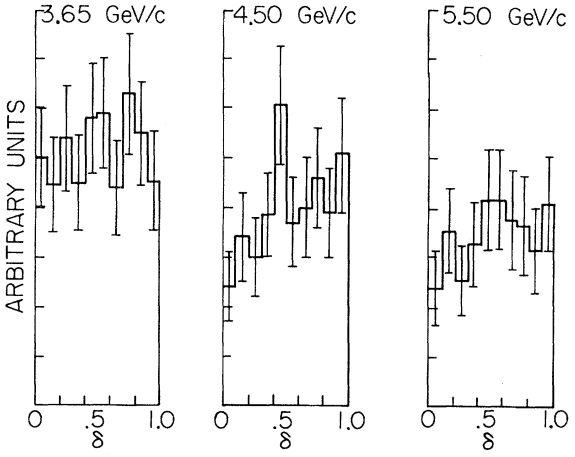

FIG. 8. The radial-Dalitz-plot density for the control region.

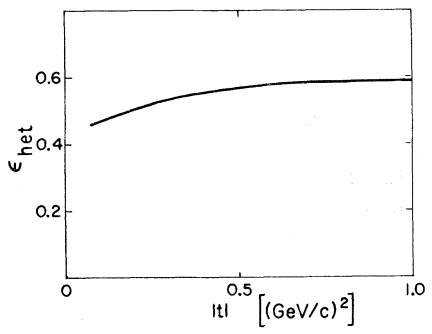

FIG. 9. The efficiency ϵ_{net}, as determined by Monte Carlo studies, for detecting and reconstructing two pions and two γ rays. The neutron-counter acceptance and efficiency is not included in ϵ_{net}.

TABLE II. Coefficients of $Y_{LM}(\theta,\phi)$ in the weighting function determined by Monte Carlo simulation. This weighting function is used to eliminate spurious alignment introduced by geometric biases.

$L \backslash M$	+4	3	2	1	0	−1	−2	−3	−4
2			0.12	0.00	0.02	0.00	0.12		
4	−0.02	0.015	0.015	0.00	−0.025	0.00	0.015	−0.015	−0.02

weak dependence on momentum transfer.

To correct for this bias, a weighting function of the form

$$W=\left[W_1+\sum_{L=2,4}\sum_{M} a_{LM}Y_{LM}(\theta,\phi)\right]^{-1}$$

(θ and ϕ are the decay angles in the Gottfried-Jackson frame) was constructed and used to assign an appropriate weight to each event. The term W_1 contains the momentum-transfer dependence and is given by

$$W_1 = 1+(0.07t-0.006/t)Y_{20}(\theta,\phi)$$

at all three energies. The coefficients a_{LM} which are shown in Table II for 4.50 GeV/c are independent of momentum transfer and change only slightly from energy to energy. If all the a_{LM}'s are small, orthogonality of the spherical harmonics precludes the need for examining either odd L values or even L values greater than four when projecting out the density-matrix elements.

E. Neutron-Counter Efficiency

The detection of neutrons in scintillation counters depends on the occurrence of nuclear interactions; consequently, the detection efficiency is expected to be energy dependent. A number of experimental studies[19-24] have shown that below a kinetic energy of 100 MeV the detection efficiency is strongly dependent on the kinetic energy and the energy threshold. The detection efficiency is observed to be relatively constant from one hundred to several hundred MeV. In this experiment the neutron kinetic energies range from 20 to 540 MeV.

A computer program has been developed by Kurz[25] to calculate the efficiency of plastic scintillators for detecting neutrons in the energy range 1 to 300 MeV. This program uses the available differential cross sections for n-p scattering and total cross sections for the various n-C channels. The response of plastic scintillator (specifically NE-102) as calculated and measured by Gooding and Pugh[26] is used in the calculation. Kurz estimates a fractional error of 10% in the calculated results and presents measured results for comparison. A number of other groups[19-24] have reported similar comparisons, and the agreement is generally adequate.

To support the use of the calculated neutron-counter efficiencies in this analysis a short experiment was performed to study the reaction $\pi^- p \to \pi^0 n$ at 1.44 GeV/c. To enhance the data rate, the distance from the neutron counters to the target was changed from 10 m to 5 m. A minor change in the electronic logic resulted in a trigger corresponding to an all-neutral final state.

Two typical time-of-flight spectra are shown in Fig. 10. Both show the "prompt" peak due to photon production in the target, and a peak due to π^0 production. One also shows an η^0 peak. Each θ bin corresponded to a unique momentum-transfer (neutron kinetic energy) interval. The expected number of counts in each θ bin was determined from the published data of Crouch *et al.*[27] The detected number of charge-exchange events was obtained from the time-of-flight spectra by using a least-squares program to fit a polynomial to the background and Gaussians to the π^0 and η^0 peaks. The observed neutron-counter efficiencies were then determined by comparing the expected with the detected counts in each θ bin.

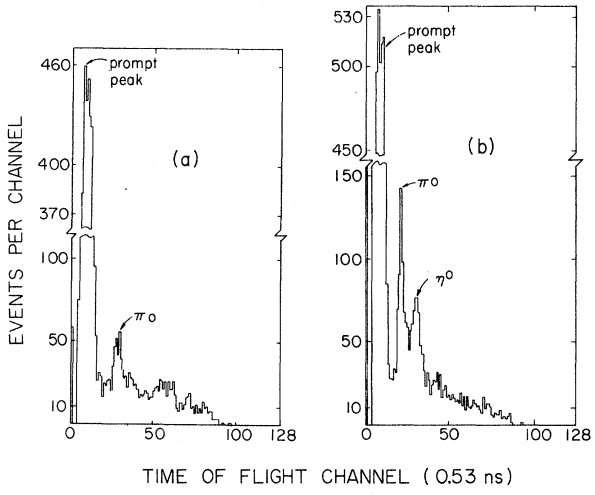

FIG. 10. Typical time-of-flight spectra obtained on-line during the $\pi^- p$ charge exchange run: (a) The prompt peak and the peak due to $\pi^- p$ charge-exchange scattering are visible, and (b) the peak due to η^0 production is also visible.

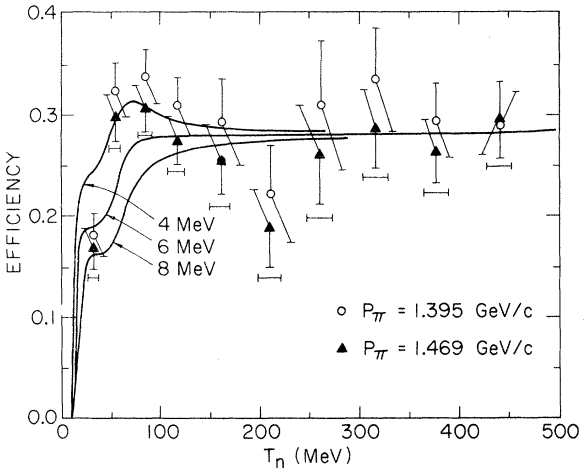

FIG. 11. Measured efficiencies based on charge-exchange data from Crouch *et al.* (Ref. 27). The curves are calculated for 4-, 6-, and 8-MeV thresholds. The horizontal bars indicate the kinetic energy interval spanned by the individual counters.

The neutron-counter thresholds were measured to be 6 MeV. In Fig. 11 the calculated efficiencies for 4, 6, and 9 MeV thresholds are shown together with our measured efficiencies based on the data of Crouch *et al.*[27] The errors include both our statistical errors and the published errors on the cross-section data. The general agreement justifies the use of the calculated efficiency. Hence, we use the results of the Kurz program to weight each event inversely by its detection probability.

IV. RESULTS AND CONCLUSIONS

In order to obtain an over-all normalization of the differential cross section independent of scanning and measuring efficiencies, we utilized the raw-unfitted-missing-mass spectra in the momentum-transfer interval $0.15 \leq |t| \leq 0.60$. Figure 12 shows this mass spectrum for the 4.50-GeV/c data. [The $\rho(765)$ is strongly suppressed in this data sample due to trigger biases against ρ's and also due to the sharp falloff in $d\sigma/dt$ for ρ's in this momentum-transfer interval. We estimate a contamination of less than 10%.] These mass spectra were fitted to a Gaussian plus a quadratic background to determine the total number of ω events, N_{spec}, detected in our spectrometer at each beam momentum. These results were then used to determine appropriate scale factors relating N_{spec} to the number remaining in the final data sample, N_{fit}. These scale factors, $N_{\text{spec}}/N_{\text{fit}}$, took into account scanning and measuring losses.

For a given momentum-transfer interval Δt, the total number of ω's produced at the target ΔN_{tot} is given by

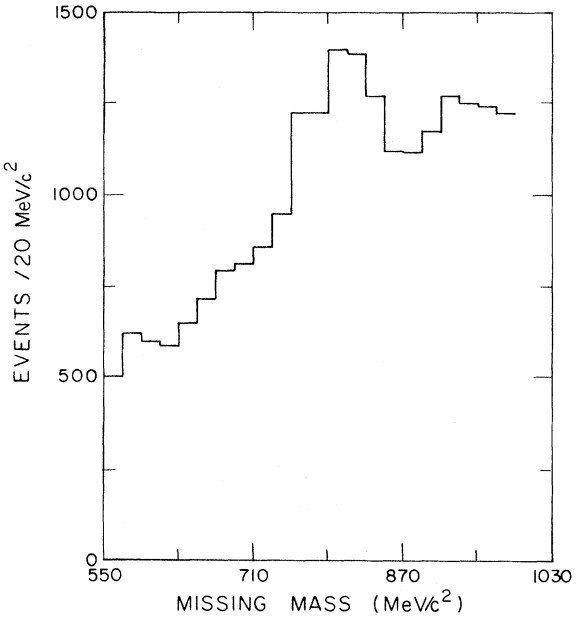

FIG. 12. The 4.50-GeV/c raw-unfitted-missing-mass spectrum for the momentum-transfer interval $0.15 < |t| < 0.60$ (GeV/c)^2. The spectra at the other momenta are similar.

$$\frac{\Delta N_{\text{tot}}}{\Delta t} = \frac{\Delta N_{\text{fit}}}{\Delta t} \left\langle \frac{N_{\text{spec}}}{N_{\text{fit}}} \right\rangle R \frac{1}{\epsilon},$$

where ΔN_{fit} is the number of fitted ω events, each weighted by the neutron-counter efficiency and the weighting function $W(\theta, \phi)$. The quantity ϵ is given by

$$\epsilon = \frac{\epsilon_{\text{net}}}{\epsilon_{2\gamma}\epsilon_{\text{prog}}},$$

where ϵ_{net}, $\epsilon_{2\gamma}$, and ϵ_{prog} are averaged over Δt. The quantity R given by

$$R = \frac{\langle \epsilon_{\text{prog}} \rangle}{\epsilon_{\text{prog}}} \frac{\langle \epsilon_{2\gamma} \rangle}{\epsilon_{2\gamma}}$$

corrects for variations in the efficiencies ϵ_{prog} and $\epsilon_{2\gamma}$ with momentum transfer. The quantities $\langle \epsilon_{2\gamma} \rangle$

TABLE III. Differential cross section in mb/(GeV/c)^2. Errors do not include the estimated 20% normalization uncertainty.

$\lvert t \rvert$ [(GeV/c)^2] \ P_{lab}	3.65 GeV/c	4.5 GeV/c	5.5 GeV/c
0.05–0.10	0.55 ± 0.14	0.44 ± 0.09	0.21 ± 0.07
0.10–0.15	0.57 ± 0.11	0.44 ± 0.07	0.38 ± 0.07
0.15–0.20	0.62 ± 0.10	0.35 ± 0.06	0.34 ± 0.06
0.20–0.25	0.78 ± 0.11	0.51 ± 0.07	0.38 ± 0.06
0.25–0.30	0.53 ± 0.09	0.41 ± 0.06	0.29 ± 0.05
0.30–0.35	0.43 ± 0.09	0.32 ± 0.05	0.23 ± 0.04
0.35–0.40	0.52 ± 0.09	0.23 ± 0.05	0.16 ± 0.03
0.40–0.50	0.38 ± 0.06	0.24 ± 0.03	0.13 ± 0.02
0.50–0.60	0.32 ± 0.04	0.16 ± 0.03	0.077 ± 0.018
0.60–0.80	0.14 ± 0.02	0.069 ± 0.013	0.047 ± 0.009
0.80–1.00	0.074 ± 0.017	0.053 ± 0.010	0.008 ± 0.005

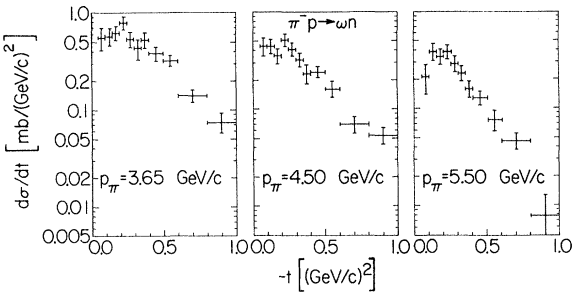

FIG. 13. The differential cross sections.

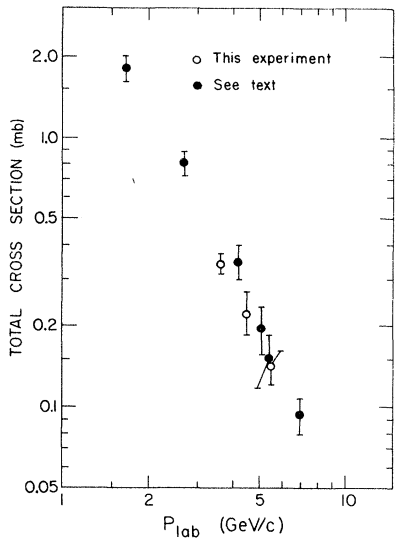

FIG. 14. The total cross section for $\pi^- p \to \omega n$ as a function of P_{lab}.

and $\langle \epsilon_{prog} \rangle$ are these efficiencies averaged over the momentum-transfer interval used in defining the scale factor. Thus, to first order, our normalization is independent of scanning and measuring efficiences and absolute values of $\epsilon_{2\gamma}$ and ϵ_{prog}.

The resulting differential cross sections are shown in Fig. 13, and are summarized in Table III. The qualitative features of these cross sections are: (1) a leveling off of $d\sigma/dt$ at low $|t|$ with the suggestion of a dip in the forward direc-

TABLE IV. Spin-density matrix elements of the ω in the reaction $\pi^- p \to \omega n$.

Density matrix elements	$\lvert t \rvert$ [(GeV/c)^2]	P_{lab} 3.65 GeV/c	4.50 GeV/c	5.50 GeV/c	3.65 GeV/c	4.50 GeV/c	5.50 GeV/c
		Gottfried-Jackson frame			Helicity frame		
ρ_{00}	0.05–0.15	0.51 ± 0.11	0.28 ± 0.09	0.33 ± 0.11	0.29 ± 0.10	0.29 ± 0.10	0.35 ± 0.12
	0.15–0.25	0.27 ± 0.07	0.33 ± 0.07	0.29 ± 0.08	0.17 ± 0.07	0.28 ± 0.08	0.22 ± 0.07
	0.25–0.35	0.20 ± 0.10	0.22 ± 0.07	0.06 ± 0.08	0.42 ± 0.10	0.25 ± 0.07	0.29 ± 0.09
	0.35–0.50	0.25 ± 0.08	0.23 ± 0.07	0.11 ± 0.09	0.32 ± 0.08	0.28 ± 0.08	0.19 ± 0.09
	0.50–0.70	0.38 ± 0.09	0.28 ± 0.09	0.36 ± 0.13	0.22 ± 0.08	0.24 ± 0.09	0.12 ± 0.12
	0.70–1.00	0.48 ± 0.13	0.40 ± 0.13	0.67 ± 0.23	0.25 ± 0.11	0.17 ± 0.13	0.20 ± 0.18
ρ_{1-1}	0.05–0.15	0.26 ± 0.10	0.20 ± 0.08	0.16 ± 0.10	0.15 ± 0.10	0.20 ± 0.08	0.17 ± 0.11
	0.15–0.25	0.17 ± 0.07	0.19 ± 0.07	0.24 ± 0.07	0.12 ± 0.07	0.17 ± 0.07	0.20 ± 0.07
	0.25–0.35	0.05 ± 0.09	0.14 ± 0.07	0.21 ± 0.08	0.16 ± 0.09	0.15 ± 0.07	0.32 ± 0.08
	0.35–0.50	0.10 ± 0.07	0.11 ± 0.07	0.27 ± 0.09	0.13 ± 0.07	0.14 ± 0.07	0.31 ± 0.09
	0.50–0.70	0.07 ± 0.08	0.10 ± 0.09	0.19 ± 0.12	−0.01 ± 0.09	0.08 ± 0.09	0.07 ± 0.12
	0.70–1.00	−0.10 ± 0.09	0.01 ± 0.12	−0.01 ± 0.16	−0.22 ± 0.11	−0.11 ± 0.12	−0.24 ± 0.20
Re(ρ_{10})	0.05–0.15	−0.04 ± 0.06	−0.04 ± 0.05	−0.06 ± 0.07	0.18 ± 0.06	0.03 ± 0.05	0.03 ± 0.06
	0.15–0.25	0.02 ± 0.04	−0.07 ± 0.04	−0.06 ± 0.04	0.00 ± 0.04	0.08 ± 0.04	0.08 ± 0.04
	0.25–0.35	−0.13 ± 0.05	−0.00 ± 0.04	−0.07 ± 0.05	0.09 ± 0.05	−0.01 ± 0.04	0.01 ± 0.05
	0.35–0.50	−0.14 ± 0.04	0.00 ± 0.04	−0.02 ± 0.05	0.13 ± 0.04	−0.02 ± 0.04	0.02 ± 0.05
	0.50–0.70	−0.12 ± 0.05	−0.11 ± 0.06	−0.10 ± 0.07	0.10 ± 0.05	0.09 ± 0.05	0.08 ± 0.07
	0.70–1.00	−0.20 ± 0.07	−0.21 ± 0.08	−0.09 ± 0.12	0.16 ± 0.07	0.17 ± 0.08	0.03 ± 0.13
		$\rho_{11} - \rho_{1-1}$ (Gottfried-Jackson frame)			$\rho_{11} + \rho_{1-1}$ (both frames)		
	0.05–0.15	−0.01 ± 0.10	0.17 ± 0.08	0.18 ± 0.10	0.51 ± 0.12	0.57 ± 0.10	0.49 ± 0.13
	0.15–0.25	0.19 ± 0.07	0.15 ± 0.07	0.12 ± 0.06	0.54 ± 0.08	0.53 ± 0.09	0.60 ± 0.09
	0.25–0.35	0.35 ± 0.09	0.25 ± 0.07	0.26 ± 0.08	0.45 ± 0.11	0.53 ± 0.08	0.68 ± 0.10
	0.35–0.50	0.28 ± 0.08	0.27 ± 0.07	0.18 ± 0.09	0.47 ± 0.08	0.50 ± 0.08	0.72 ± 0.11
	0.50–0.70	0.24 ± 0.09	0.25 ± 0.09	0.12 ± 0.13	0.38 ± 0.10	0.46 ± 0.11	0.51 ± 0.14
	0.70–1.00	0.36 ± 0.11	0.29 ± 0.13	0.17 ± 0.18	0.16 ± 0.12	0.31 ± 0.14	0.16 ± 0.22

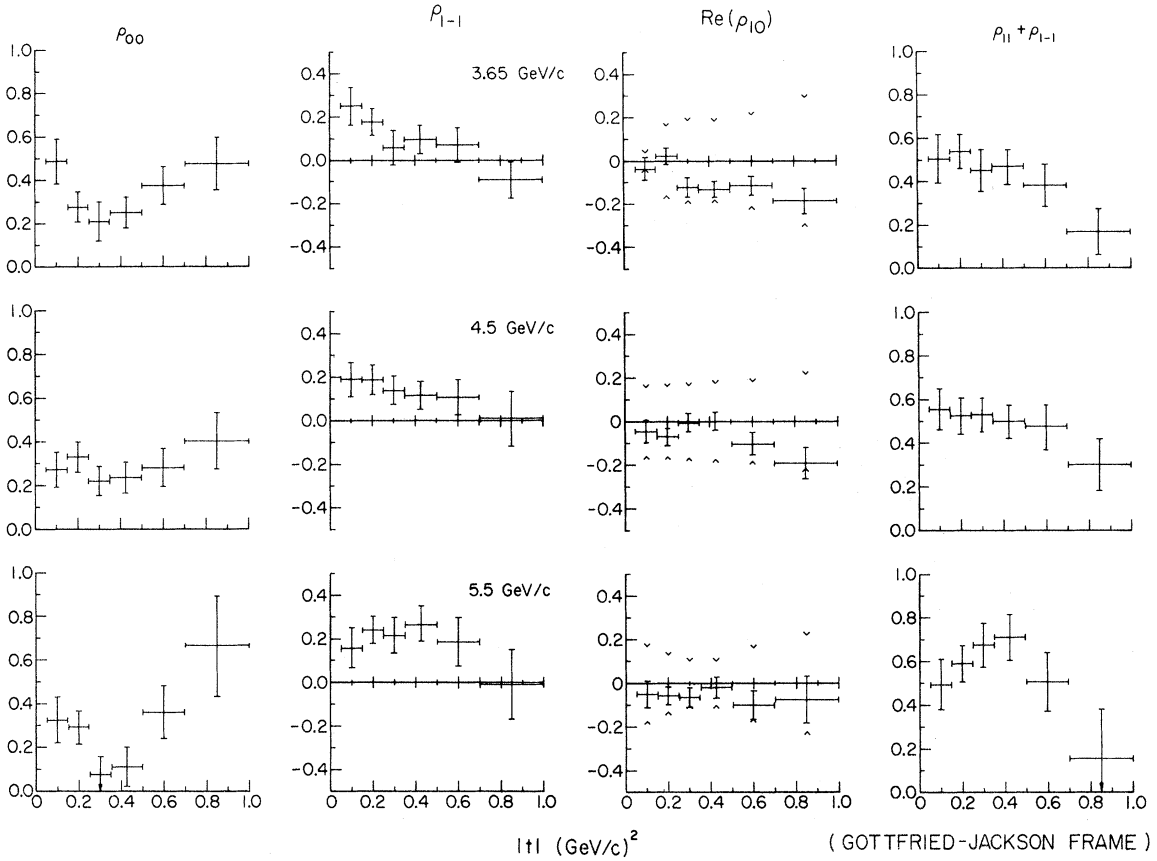

FIG. 15. The ω spin-density matrix elements.

tion at the highest energy; (2) smooth falloff with increasing $|t|$ beyond 0.25 (GeV/c)^2; and (3) no evidence for a dip in $d\sigma/dt$ at $|t|$ near 0.6 (GeV/c)^2. These features are in agreement with the previously reported data. A fit of $d\sigma/dt$ to the form Ae^{Bt} in the momentum-transfer interval $0.25 < |t| < 1.0$ (GeV/c)^2 gives $B = 3.2 \pm 0.3$, 3.6 ± 0.3, and 4.9 ± 0.5 (GeV/c)$^{-2}$ at 3.65, 4.50, and 5.50 GeV/c, respectively.

Figure 14 shows the total cross sections σ_T, of our results and of other experiments.[4-11] In computing the total cross sections at each energy we summed the differential cross sections over the momentum-transfer interval $0.05 \leq |t| \leq 1.0$ (GeV/c)^2 and added a contribution to correct for the unobserved interval $0.0 \leq |t| \leq 0.05$ (GeV/c)^2. This contribution was taken to be 90% of that in the region $0.05 \leq |t| \leq 0.10$ (GeV/c)^2. No contributions were added for $|t| \leq 1.0$ (GeV/c)^2.

The ω spin-density matrix elements were evaluated for each momentum-transfer interval by using a moment-analysis technique to project our various components of the angular distributions. The control regions described in Sec. III C were used to subtract background.

The results are presented in Fig. 15 and Table IV. We note two important features of these data: (1) The density matrix elements ρ_{00} and $\rho_- \equiv \rho_{11} - \rho_{1-1}$ are large, thus implying unnatural-parity exchange contributions. (2) The large value of

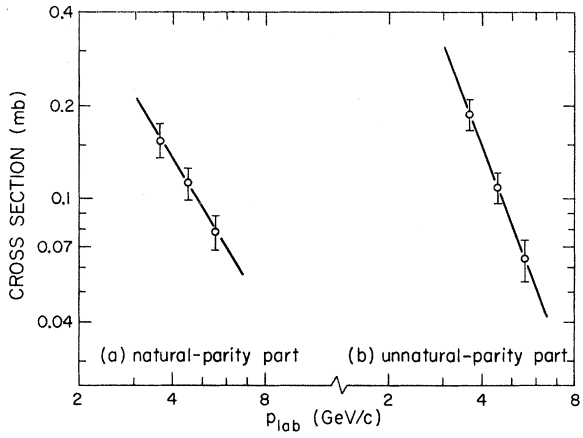

FIG. 16. The dependence of the natural- and unnatural-parity parts of the total cross section on the incident beam momentum.

$\rho_+ \equiv \rho_{11} + \rho_{1-1}$ at $|t| \sim 0.6$ (GeV/c)^2 implies that either the ρ trajectory is not the sole natural-parity contribution to the process or there is no wrong-signature nonsense zero in the ρ-trajectory contribution to the scattering amplitude. See Ref. 1 for a more complete discussion.

The energy dependences of the natural- and unnatural-parity parts of the total cross section are shown in Fig. 16. Here, the natural- and unnatural-parity parts of the differential cross section are defined by

$$\sigma_n = \int \frac{d\sigma_n}{dt}\, dt$$

$$= \int (\rho_{11} + \rho_{1-1}) \frac{d\sigma}{dt}\, dt$$

and

$$\sigma_u = \int \frac{d\sigma_u}{dt}\, dt$$

$$= \int [\rho_{00} + (\rho_{11} - \rho_{1-1})] \frac{d\sigma}{dt}\, dt \,.$$

If we assume an s dependence for these cross sections of the form $s^{2\alpha(0)-2}$, then a fit to our data gives $\alpha_n(0) = 0.3 \pm 0.3$ and $\alpha_u(0) = -0.3 \pm 0.4$ for the natural- and unnatural-parity cases, respectively. The commonly accepted value of the intercept of the ρ trajectory is $\alpha_\rho(0) \sim 0.5$; of the B trajectory, $\alpha_B(0) \sim -0.3$ to -0.5.

We conclude that the energy dependence of the data is consistent with that expected from simple Regge models. However, the fact the ρ_+ is large at $|t| \sim 0.6$ (GeV/c)^2 disagrees strongly with the predictions of these models.

ACKNOWLEDGMENTS

We wish to acknowledge the help of the Zero-Gradient Synchrotron and Argonne Applied Mathematics Division staffs, our engineers and technicians, the scanning and measuring crews, and the staff of our 7094 computer. We also express our thanks to Argonne National Laboratory for the neutron-counter hodoscope, to James H. Smith, Robert Cullum, and David Eitelbach for their assistance with the XDS $\Sigma 2$, to T. Novey, D. Lundquist, and H. Frauenfelder for help in the early phase of the experiment, and to Lorella Jones and Roy Schult for many helpful conversations on the theoretical framework.

---

*Work supported in part by the U. S. Atomic Energy Commission.

†Present address: 15 Alpine St., Cambridge, Massachusetts.

‡Present address: Department of Physics, Northeastern University, Boston, Massachusetts 02115.

§Present address: Telemed, Chicago, Illinois.

‖Present address: University of Chicago, Enrico Fermi Institute, Chicago, Illinois 60637.

**Present Address: Department of Physics, Cornell University, Ithaca, New York 14850.

††Present address: Adelphi University, Garden City, New York 11530.

[1]L. E. Holloway, B. Huld, M. Jordan, D. W. Mortara, E. I. Rosenberg, A. D. Russell, S. Bernstein, M. H. Garrell, S. Margulies, and D W. McLeod, Phys. Rev. Lett. 27, 1671 (1971).

[2]In these and further discussions we refer to the coordinate system described by K. Gottfried and J. D. Jackson [Nuovo Cimento 33, 309 (1964)].

[3]J. P. Ader, M. Capdeville, G. Cohen-Tannoudji, and Ph. Salin, Nuovo Cimento 56A, 952 (1968); H. Hogaasen and H. J. Lubatti, Phys. Lett. 26B, 166 (1968).

[4]1.7 GeV/c: T. C. Bacon, W. J. Fickinger, D. G. Hill, H. W. K Hopkins, D. K. Robinson, and E. O. Salant, Phys. Rev. 157, 1263 (1967).

[5]2.7 GeV/c: R. J. Miller, S. Lichtman, and R. B. Willmann, Phys. Rev. 178, 2061 (1969).

[6]3.2 GeV/c: H. O. Cohn, W. M. Bugg, and G. T. Condo, Phys. Lett. 15, 344 (1965).

[7]3.65 GeV/c: G. C. Benson, B. P. Roe, D. Sinclair, and J. C. Vander Velde, Phys. Rev. Lett. 22, 1074 (1969).

[8]4.2 GeV/c: G. S. Abrams, B. Eisenstein, and H. Gordon, Phys. Rev. Lett. 23, 673 (1969).

[9]5.1 GeV/c: N. Armenisi, B. Ghidini, V. Picciarelli, A. Romano, A. Silvestri, A. Forino, R. Gessaroli, L. Lendinara, A. Quareni-Vignudelli, A. Cartacci, M. G. Dagliana, G. di Caporiacco, M. Barrier, D. Mettel, and J. Quinquard, Nuovo Cimento 65A, 637 (1970).

[10]5.4 GeV/c: M. S. Farber, J. V. DePinto, N. N. Biswas, N. M. Cason, B. J. Deery, V. P. Kenny, J. A. Poirier, O. R. Sander, and W. D. Shephard, Nucl. Phys. B29, 237 (1971).

[11]6.95 GeV/c: J. A. J. Matthews, J. D. Prentice, T. S. Yoon, J. T. Carroll, M W. Firebaugh, and W. D. Walker, Phys. Rev. Lett. 26, 400 (1971).

[12]Flight Research, Inc., subsidiary of the Giannini Scientific Corp., Richmond, Virginia.

[13]Nuclear Enterprises, Ltd., Winnipeg, Manitoba, Canada.

[14]EG & G., Oak Ridge, Tennessee.

[15]LeCroy Research Systems, West Nyack, New York.

[16]Xerox Digital Systems, El Segundo, California.

[17]Kennedy Co., Pasadena, California.

[18]R. W. Downing, D. W. Mortara, and C. A. Schaad, University of Illinois report, 1966 (unpublished).
[19]C. E. Wiegand, T. Elioff, W. B. Johnson, L. B. Auerbach, J. Lach, and T. Ypsilantis, Rev. Sci. Instrum. 33, 526 (1962).
[20]G. Gatti, P. Hillman, W. C. Middelkoop, T. Yamagata, and E. Zavattini, Nucl. Instrum. Methods 29, 77 (1964).
[21]D. G. Crabb, J. G. McEwen, E. G. Auld, and A. Langsford, Nucl. Instrum. Methods 48, 87 (1967).
[22]C. Gewinger, Diplomarbeit, Universität Hamburg, 1967 (unpublished).
[23]D. Bollini, A. Buhler-Broglin, P. Dalpiaz, T. Massam, F. Navach, F. L. Navarria, M. A. Schneegans, F. Zetti, and A. Zichichi, Nuovo Cimento 61A, 125 (1969).
[24]J. B. Hunt, C. A. Baker, C. J. Batty, P. Ford, E. Friedman, and L. E. Williams, Nucl. Instr. Methods 85, 269 (1970).
[25]R. J. Kurz, LBL Report No. UCRL-11339, 1964 (unpublished).
[26]T. J. Gooding and H. G. Pugh, Nucl. Instrum. Methods 7, 189 (1960).
[27]H. R. Crouch, Jr., R. Hargraves, R. E. Lanou, Jr., J. T. Massimo, A. E. Pifer, A. M. Shapiro, M. Wigdoff, A. E. Brenner, M. Ioffredo, F. D. Rudnick, G. Calvelli, F. Gasparini, L. Guerriero, G. A. Salandin, A. Tomasin, C. Voci, F. Waldner, Y. Eisenberg, E. E. Ronat, S. Toaff, P. Bastien, B. Brabson, B. T. Feld, V. Kistiakowski, Y. Goldschmidt-Clermont, D. Miller, I. A. Pless, A. Rogers, L. Rosenson, L. Ventura, T. L. Watts, and R. K. Yamamoto, Phys. Rev. Lett. 21, 849 (1968).

PHYSICAL REVIEW D VOLUME 8, NUMBER 9 1 NOVEMBER 1973

Total Hadronic Photoabsorption Cross Sections of Nuclei for Photons in the GeV Energy Range

G. R. Brookes, A. S. Clough,* J. H. Freeland,† W. Galbraith, and A. F. King
Department of Physics, The University, Sheffield, Yorkshire, England

T. A. Armstrong, W. R. Hogg, G. M. Lewis, and A. W. Robertson‡
Department of Natural Philosophy, The University, Glasgow, Scotland

W. R. Rawlinson, N. R. S. Tait, J. C. Thompson, and D. W. L. Tolfree
Daresbury Nuclear Physics Laboratory, Daresbury, Cheshire, England
(Received 28 March 1973)

The total hadronic photoabsorption cross sections of a number of nuclei (C, Al, Cu, Nb, Sn, Ta, Pb) have been studied in detail using a tagged photon beam over the energy range 1.7–4 GeV. The results are described, and compared with models of photoabsorption.

I. INTRODUCTION

The hadronic nature of the interactions of photons in the GeV energy region with nucleons has been studied by measuring the total photoabsorption cross section (σ_T) for hadron production in hydrogen[1,2,3] and deuterium.[1,2,4] Typically, the value of the total cross section in hydrogen in this energy region is ~120 μb, which, in terms of nuclear matter, would imply a mean free path for interaction of the order of hundreds of fermis. Consequently, the photoabsorption cross section for nuclei might, naively, be expected to increase linearly with A, and a measurement of σ_T for complex nuclei is of interest to check this conclusion.

On the other hand, there is now a considerable body of evidence that many of the features of the photoproduction of hadrons off nucleons can be accounted for by the vector-meson dominance (VMD) model[5,6] in which the hadronic interaction of the photon and nucleon is mediated through a vector meson (ρ, ω, ϕ). This meson has a strong interaction with the nucleon, and consequently, one is led to expect some overshadowing of the interior nucleons by other surface nucleons, such that σ_T varies as A^x, where x could be as low as 0.7, this value being dependent upon the detailed model for the absorption of the photon and upon the photon energy. Some measurements[7,8] have already been reported from other laboratories which indicate that $x \sim 0.9$, i.e., the exponent lies in value between that predicted by the VMD model and that based on zero shadowing of the nucleons. However, essential features of the theory such as the distinct increase of shadowing with energy